RSC Advances

PAPER

View Article Online
View Journal | View Issue

Cite this: *RSC Adv.*, 2019, **9**, 41549

A step forward in the development of superoxide dismutase mimetic nanozymes: the effect of the charge of the surface on antioxidant activity†

Álvaro Martínez-Camarena, [a] José M. Llinares, [ab] Antonio Domenech-Carbó, [c] Javier Alarcón [d] and Enrique García-España *[a]

Received 31st October 2019
Accepted 7th December 2019

DOI: 10.1039/c9ra08992f

rsc.li/rsc-advances

Two binucleating hezaaza macrocycles containing a pyridinol spacer have been prepared and characterised. Protonation studies indicate the deprotonation of the phenol group at relatively low pH values with the concomitant occurrence of a keto-enolic equilibrium. These ligands readily form binuclear Cu^{2+} and Zn^{2+} complexes as denoted by potentiometric and spectroscopic studies. The binding of the metals yields to the ready deprotonation of the phenol with the stabilisation of the keto form that results in complexes of greater stabilities than the analogous ones containing pyridine as spacer instead of pyridine. Mixed Cu^{2+}–Zn^{2+}-complexes were also detected in aqueous solutions containing equimolar amounts of Cu^{2+}, Zn^{2+} and ligands. The binuclear Cu^{2+} complexes show significant SOD activity as proved by the McCord–Fridovich assays. The binuclear Cu^{2+} complexes of the ligands grafted to boehmite nanoparticles (BNPs) show a remarkable increase in SOD activity, which reaches 8-fold in one of the systems. The observed increase can be ascribed to the positive ζ-potential of the BNPs since the same complexes anchored to silica nanoparticles with negative ζ-potential do not show any apparent increase in activity. This behaviour is reminiscent of the positively charged funnel found in CuZnSOD, which has the electroactive copper ion at its end.

Introduction

It is well-known that the imbalance between the production and removal of reactive oxygen species in living systems generates oxidative stress, which is related to the occurrence of neurological disorders and, therefore, has profound consequences in aging and hence in life expectancy.[1–4] Removal of excess amounts of oxygen reactive species (ROS) is carried out in healthy organisms by a battery of enzymes starting by the superoxide dismutase (SOD) family.[5] SOD enzymes take care of the dismutation reaction of superoxide anionic radicals into dioxygen and hydrogen peroxide, which is then transformed into dioxygen and water by the action of the catalase family of enzymes (CATs).[6,7] Although natural enzymes might be employed to remove ROS excesses,[8–10] this procedure suffers from severe drawbacks such as lack of oral activity, immunogenicity, short half-life and low cell permeability.[11,12] Therefore, low-molecular weight mimetics may be better suited than natural enzymes for this purpose owing to their lack of antigenicity, good tissue penetrance, high stability, longer half-life in solution, and low production cost.[13,14] A number of these low molecular SOD mimetics are complexes of polyamine ligands of either cyclic or acyclic topology.[15–20] In this respect, we have recently reported that several mononuclear or binuclear manganese and copper complexes of aza-macrocyclic ligands have SOD activities *in vitro* which rank among the highest ones so far reported for synthetic systems.[21–23]

A plausible way of increasing SOD activity might be the attachment of the molecules to the surface of appropriate nanoparticles (NPs). Regarding this point, we have recently communicated that the Cu^{2+} binuclear complexes of the hexaazapyridinophane ligand **L1** (Scheme 1) exhibited an 8-fold enhanced SOD activity when grafted to boehmite nanoparticles (BNPs).[24] The reason for such a behaviour was in principle related to the accumulation of active sites in the surface of the BNPs.[25] However, other factors may also influence the observed behaviour such as the charge of the nanoparticle surface. Boehmite has typically a positively charged surface that may attract the negatively charged superoxide anions towards the electroactive centres. This behaviour is somehow reminiscent of the funnel found in Cu_2Zn_2SOD, which has the electroactive copper ion at its end, and displays a gradient of increasing

[a]*ICMol, Departamento de Química Inorgánica, Universidad de Valencia, C/Catedrático José Beltrán 2, 46980, Paterna, Spain. E-mail: enrique.garcia-es@uv.es*
[b]*Departamento de Química Orgánica, Universidad de Valencia, C/Dr Moliner s/n, 46100, Burjassot, Spain*
[c]*Departamento de Química Analítica, Universidad de Valencia, C/Dr Moliner s/n, 46100, Burjassot, Spain*
[d]*Departamento de Química Inorgánica, Universidad de Valencia, C/Dr Moliner s/n, 46100, Burjassot, Spain*

† Electronic supplementary information (ESI) available: Complete experimental procedure, supplementary NMR figures and analysis. See DOI: 10.1039/c9ra08992f

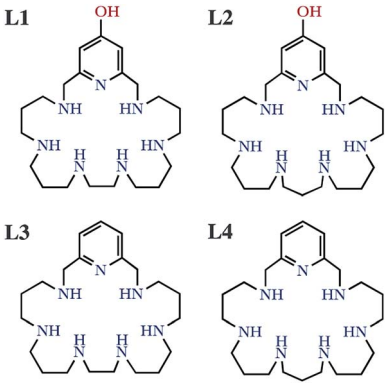

Scheme 1 Drawing of the ligands studied in this work.

positive charge as the funnel approaches the electroactive centre.[5,26] Herein we have prepared a novel hexazacyclophane receptor containing a continuous set of propylene chains between the amine groups linked to the 2,6-positions of a pyridinol ring through methylene groups (**L2**). We compare its Cu^{2+} and Zn^{2+} coordination behaviour with that of the parent ligand **L1** and with those of the ligands having pyridine instead of pyridinol groups (**L3** and **L4** in Scheme 1). Moreover, we have grafted the new ligand to the surface of BNPs and we have estimated the SOD activity of the new system. In order to evaluate the influence the charge of the surface of the NPs we have measured the ζ-potential of either the BNPs alone or the BNPs grafted with either only the ligand or with 1 : 1 or 2 : 1 molar ratios of Cu^{2+}. Finally, we have compared these systems with analogous ones in which we have attached our ligands to silica NPs (SNPs) that supposedly have a negatively charged surface.

Results and discussion

Synthetic procedures

L2 has been synthesised in good yield by means of a modification of the Richman–Atkins procedure[27] in which the tosylated amine 1,5,9,13,17,21-hexakis(ρ-tolylsulfonyl)-1,5,9,13,17,21-hexaazaheneicosane[28,29] was reacted with 4-(benzyloxy)-2,6-bis(chloromethyl)pyridine[30,31] in CH_3CN using K_2CO_3 as a base. The removal of the tosyl and benzyl groups was performed using HBr/AcOH with an excess of phenol. Characterisation data of the compound are included in the ESI (Fig. S1–S6).†

Boehmite nanoparticles (BNPs) were prepared by a two-step procedure already described.[32] In the first step aluminium *tert*-butoxide was hydrolysed at 85 °C in water under strong stirring. After the alkoxide addition, a gel was formed almost instantaneously. In the second step a peptization process was carried out keeping the BNPs in HNO_3 for several days at 95 °C. Characterization data of both the boehmite and the silica nanoparticles are included in the ESI (Fig. S7 and S8).†

The grafting of the macrocycles to the BNPs or SNPs was performed by condensation of the pyridinol groups with the terminal Al–OH or Si–OH groups at the surface of the nanoparticles. The amount of grafted macrocycle was measured by elemental microanalysis and ^1H NMR using TSP as internal standard. The values obtained were $[\mathbf{L1}] = (3.5 \pm 0.4) \times 10^{-5}$ mol g_{BNP}^{-1} and $[\mathbf{L2}] = (2.20 \pm 0.02) \times 10^{-4}$ mol g_{BNP}^{-1} for the functionalised boehmite nanoparticles and $[\mathbf{L1}] = (2.3 \pm 0.2) \times 10^{-5}$ mol g_{SNP}^{-1} and $[\mathbf{L2}] = (3.3 \pm 0.3) \times 10^{-5}$ mol g_{SBP}^{-1} for the grafted silica ones (see Table S1 and Fig. S9–S18 in the ESI†). Furthermore, ICP-MS analysis showed that there were two moles of copper by every mole of grafted ligand (see ESI, Table S1†).

Table 1 Logarithms of the stepwise protonation constants for **L1**[24] and **L2** obtained by potentiometric measurements. The constants were determined in 0.15 M $NaClO_4$ at 298.1 ± 0.1 K

Reaction	**L1**[24]	**L2**
$H_{-1}L^- + H^+ \rightleftarrows H(H_{-1}L)$	10.68(2)[a]	10.03(2)
$H(H_{-1}L) + H^+ \rightleftarrows H_2(H_{-1}L)^+$	10.11(2)	9.98(1)
$H_2(H_{-1}L)^+ + H^+ \rightleftarrows H_3(H_{-1}L)^{2+}$	9.36(1)	8.99(2)
$H_3(H_{-1}L)^{2+} + H^+ \rightleftarrows H_4(H_{-1}L)^{3+}$	7.97(1)	7.94(2)
$H_4(H_{-1}L)^{3+} + H^+ \rightleftarrows H_5(H_{-1}L)^{4+}$	6.13(1)	6.61(2)
$H_5(H_{-1}L)^{4+} + H^+ \rightleftarrows H_5L^{5+}$	5.81(1)	6.03(2)
$H_5L^{5+} + H^+ \rightleftarrows H_6L^{6+}$	4.14(2)	5.09(4)
$\log \beta^b$	54.20	54.67

[a] Values in parentheses are standard deviations in the last significant figure. [b] $\log \beta = \sum \log K$.

Acid-base behaviour

The protonation constants of **L2** obtained by potentiometric titrations, as well as those we have previously reported for **L1**,[24] are shown in Table 1. The representation of the distribution diagrams as a function of the pH are shown in Fig. 1. The

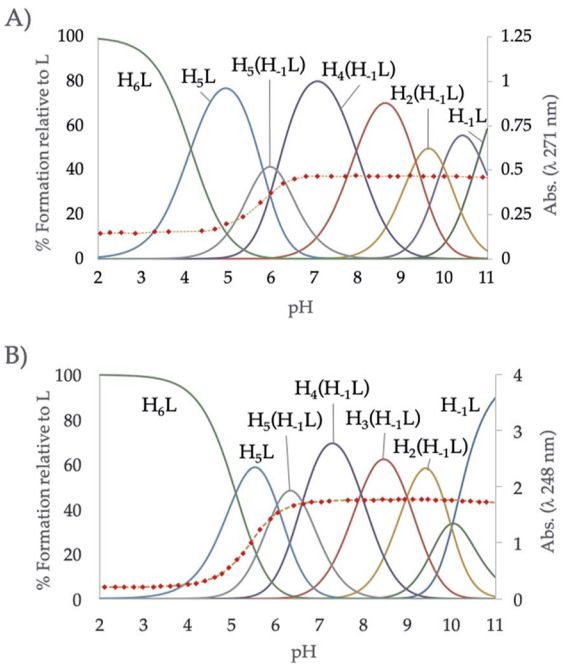

Fig. 1 Distribution diagram of (A) **L1** and (B) **L2** as a function of the pH in aqueous solution. The absorbance at 248 nm in the UV-Vis spectra is represented overlaid as diamonds (◆).

protonation constants for the related pyridine containing cyclophanes **L3** and **L4**, as well as their distribution diagrams, are collected in Table S2, Fig. S19 and S20 of the ESI.†

The potentiometric titrations allowed to determine 7 protonation constants ranging from 10.03 to 5.09 logarithmic units (Table 1). **L2** follows the typical protonation behaviour usually found for cyclic polyamines, already shown for **L1**, which is based on the electrostatic repulsions between protonated amino groups, inductive effects of the alkyl and aromatic groups and statistic effects.[29,33] The differences between the protonation constant values of **L1** and **L2**,[24] can be explained according to minimisation of charge repulsions and inductive effects.

L1, which has an ethylenic chain at the centre of the polyamine bridge, shows higher constant values for the first protonation steps, and smaller values for the last ones than **L2**. This effect can be explained attending to the separation between the amino groups in each ligand and its influence on intramolecular interactions. While the shorter ethylenic chains favours the stabilisation of the first protonations promoting the formation of intramolecular hydrogen bonds, the longer propylenic chains minimise the electrostatic repulsions in the last protonations.[34]

On the other hand, a comparison between the ligands with pyridinol or pyridine group and the same chain **L1** *vs.* **L3** and **L2** *vs.* **L4** (see Table S2 in the ESI†), reveals that the first constants of the pyridinol ligands, **L1** and **L2**, show higher values than those corresponding to the pyridine receptors, **L3** and **L4**, excluding the first protonation of **L2**. However, it is interesting to note that this tendency is reversed with the fourth protonation. Registration of the UV spectra at variable pH can give an explanation for this effect. While for the pyridine macrocycles **L3** and **L4** the band of the aromatic spacer at ~260 nm does not change with pH, for the pyridinol ones it experiments a very significant hypochromism from pH 7 to 5 (Fig. 1). This can be attributed to the protonation of the phenolate that would occur coupled to the formation of the H_5L^{5+} species, $H_5(H_{-1}L)^{4+} + H^+ \rightleftarrows H_5L^{5+}$ equilibrium. Deprotonation of the pyridinol moiety gives rise to a keto-enolic equilibrium (Fig. 2) whose ketonic form presents a negative charge located on the pyridinic nitrogen. Thus, the removal of the enolic hydrogen observed by the UV titrations could stabilise the first four protonations of the receptors through the formation of intramolecular ionic interactions (salt bridges), increasing the value of their constants.

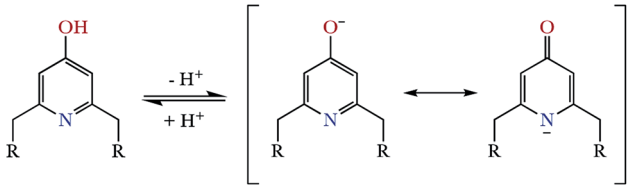

Fig. 2 Representation of the keto-enolic equilibrium determined for the pyridinolic moiety.

Cu^{2+} complexation

The Cu^{2+} complexation constants of **L2** determined by potentiometric titrations, as well as those of **L1**,[24] are shown in Table 2. The stability constants of the pyridinophane ligands **L3** and **L4**,[29] are collected in Table S3 of the ESI.†

The speciation studies show the formation of mononuclear $[CuH_x(H_{-1}L)]^{(1+x)+}$ species with x ranging from 0 to 5 and binuclear species of $[Cu_2H(H_{-1}L)]^{4+}$, $[Cu_2(H_{-1}L)]^{3+}$, $[Cu_2(H_{-1}L)(OH)]^{2+}$ and $[Cu_2(H_{-1}L)(OH)_2]^{+}$ stoichiometries. The distribution diagrams collected in Fig. 3 (and in Fig. S21–S26 in the ESI†) show that, while for Cu^{2+} : L 1 : 1 mole ratio only mononuclear species are present in solution in the pH covered in the studies (2.5–11.0), for a 2 : 1 ratio the binuclear species prevail above pH 4 for **L1** and above pH 6 for **L2**. Although inferring coordination numbers and geometries just from the stability constants values could be highly misleading, the combined analysis of these results with UV spectra recorded at variable pH of solutions with different Cu^{2+} : L mole ratios can give useful information. Thus, the variation of the pyridine band, centred at ~260 nm, with pH for solutions with either 1 : 1 or 2 : 1

Table 2 Logarithms of the equilibrium constants for the interaction of Cu^{2+} with **L1**[24] and **L2** obtained by potentiometric measurements. The logarithms constants were determined in 0.15 M $NaClO_4$ at 298.1 ± 0.1 K

Entry	Reaction	**L1**[24]	**L2**
1	$[CuH_4(H_{-1}L)]^{5+} + H^+ \rightleftarrows [CuH_5(H_{-1}L)]^{6+}$	3.79(6)[a]	4.13(2)
2	$[CuH_3(H_{-1}L)]^{4+} + H^+ \rightleftarrows [CuH_4(H_{-1}L)]^{5+}$	5.04(7)	5.22(2)
3	$[CuH_2(H_{-1}L)]^{3+} + H^+ \rightleftarrows [CuH_3(H_{-1}L)]^{4+}$	4.35(7)	6.30(4)
4	$[CuH(H_{-1}L)]^{2+} + H^+ \rightleftarrows [CuH_2(H_{-1}L)]^{3+}$	6.16(4)	7.34(4)
5	$[Cu(H_{-1}L)]^{+} + H^+ \rightleftarrows [CuH(H_{-1}L)]^{2+}$	8.24(4)	9.22(6)
6	$H_{-1}L^{-} + Cu^{2+} \rightleftarrows [Cu(H_{-1}L)]^{+}$	23.56(4)	19.25(4)
7	$[Cu(H_{-1}L)]^{+} + H_2O \rightleftarrows [Cu(H_{-1}L)(OH)] + H^+$	−10.11(5)	−10.71(3)
8	$[Cu(H_{-1}L)]^{+} + Cu^{2+} \rightleftarrows [Cu_2(H_{-1}L)]^{3+}$	8.80(4)	6.95(6)
9	$[Cu_2(H_{-1}L)]^{3+} + H_2O \rightleftarrows [Cu_2(H_{-1}L)(OH)]^{2+} + H^+$	−7.26(6)	−6.89(2)
10	$[Cu_2(H_{-1}L)(OH)]^{2+} + H_2O \rightleftarrows [Cu_2(H_{-1}L)(OH)_2]^{+} + H^+$	−8.20(6)	−9.90(1)
11	$Cu^{2+} + H(H_{-1}L) \rightleftarrows [CuH(H_{-1}L)]^{2+}$	21.11(4)	18.44(6)
12	$2Cu^{2+} + H(H_{-1}L) \rightleftarrows [Cu_2H(H_{-1}L)]^{4+}$	26.44(4)	—
13	$[CuH(H_{-1}L)]^{2+} + Cu^{2+} \rightleftarrows [Cu_2H(H_{-1}L)]^{4+}$	5.33(4)	—

[a] Values in parentheses are standard deviations in the last significant figure.

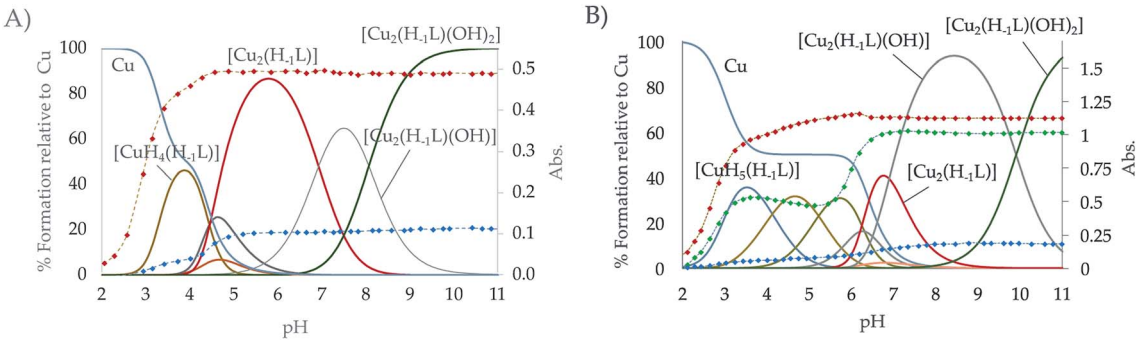

Fig. 3 Distribution diagram of the Cu^{2+} : L systems for the ligands (A) **L1** and (B) **L2** as a function of the pH in aqueous solution ($[Cu^{2+}] = 2 \times 10^{-3}$ M; $[L] = 10^{-3}$ M). The UV-Vis spectroscopic parameters of the pyridine system (red dots, $\lambda = 285$ nm for the Cu^{2+} : **L1** system and 281 nm for Cu^{2+} : **L2**), d–d transition band (blue dots, $\lambda = 590$ nm for the Cu^{2+} : **L1** system and 606 nm for Cu^{2+} : **L2**) and the ligand to Cu^{2+} charge transfer band for **L2** are overlaid (green dots, $\lambda = 314$ nm).

Cu^{2+} : L mole ratio show that deprotonation of the pyridinol group takes place as soon as the first Cu^{2+} binds the macrocycle, which suggests that the pyridine nitrogen atom takes part in the coordination of the metal ions since the very beginning. This observation, along with the keto-enolic equilibrium of the pyridinol moiety, could explain the higher values of the constants for the formation of the $[Cu(H_{-1}L)]^+$ species shown by **L1** and **L2** (entry 6 in Table 2) in comparison with the pyridine ones ($Cu^{2+} + L = CuL^{2+}$, $\log K = 18.34$ and 17.22 for **L3** and **L4**, respectively).[24,29] The pCu^{2+} values calculated for $[L] = 1 \times 10^{-5}$ M and $[Cu^{2+}] = 2 \times 10^{-6}$ M confirm that the pyridinol complexes are more stable than the pyridine ones, being **L1** the ligand that forms the most stable complexes (Fig. S27†).[35] DFT calculations performed for the complex $[Cu(H_{-1}\mathbf{L1})]^+$ support this point since they show as most stable the complex in which the Cu^{2+} will be bound to the nitrogen of the aromatic moiety and to four secondary amines of the chain in a square pyramidal geometry (see Fig. S28†).

The equilibrium constants found for the formation of the binuclear complexes from the mononuclear ones (entry 8 in Table 2) are rather low, suggesting either the participation of a lower number of nitrogen atoms in the coordination sphere of the second metal or a rearrangement of the coordination sites involving bond breaking and forming as DFT calculation on these systems indicate (see Fig. S28†). The variation of the spectra of the systems Cu^{2+}–**L2** and Cu^{2+}–**L1** in the UV region suggests the implication of the pyridinol ring in coordination as soon as the first complexes are formed. Coordination of the pyridinol group should lead to the deprotonation of the phenol group and to the formation of the quinone that would afford an increase of electron density on the donor group. The variation with pH of the spectra in the visible region show a profile with two plateaus corresponding to the formation of the mon- and binuclear complexes with extinction coefficients of *ca.* 123 and 339 M^{-1} cm^{-1}, respectively. On the other and, the rather acidic values of the constants for the first hydrolysis of the $[Cu_2(H_{-1}L)]^{3+}$ complexes (entry 9 in Table 2) support that the hydroxide anion is placed between the metal centres as a bridging ligand.

Zn^{2+} complexation

Since Zn^{2+} is also present in the active centre of Cu_2Zn_2SOD we next performed speciation studies for the binary Zn^{2+} : L systems. The complexation constants of **L2** obtained by potentiometric titrations, as well as those we have previously reported for **L1**,[24] are shown in Table S4.† The stability constants of the pyridinophane ligands **L3** and **L4**,[29] are collected in Table S5 of the ESI.†

The distribution diagrams collected in Fig. 4 (and in Fig. S29–S34 in the ESI†) show that, analogously to Cu^{2+} although with a reduced range of protonation degrees and lower stabilities, different mono- and binuclear complexes are formed for both systems. As observed for Cu^{2+}, the constant for the formation of the $[Zn(H_{-1}L)]^+$ is greater for **L1** than for **L2**. However, in this case while the stability constant of the $[Zn(H_{-1}\mathbf{L2})]^+$ is greater than that of its analogue pyridine receptor **L3**, the opposite situation is found for **L2** and **L4**.

Cu^{2+}–Zn^{2+} complexation

Finally, the formation of mixed Cu^{2+}–Zn^{2+}–L complexes was investigated by potentiometry. To do so, solutions containing equimolar amounts of Cu^{2+}, Zn^{2+} and of each one of the ligands were titrated with NaOH. To treat the data, as outlined in the Experimental section, in the first run the protonation and stability constants of the binary M^{2+}–L systems already determined, were introduced as fixed parameters and the constants of the mixed Cu^{2+}–Zn^{2+}–L complexes were refined. In a second run, all titrations of both the binary Cu^{2+}–L or Zn^{2+}–L and ternary Cu^{2+}–Zn^{2+}–L systems were treated together refining, in this run, the constants of all the complexes formed independently if they were binary or ternary. The values obtained were self-consistent (Table 3); the differences observed with those constants derived only from the individual titrations fell within the standard deviations. As can be seen in the distribution diagrams (Fig. 5), the mixed systems predominate in both systems above pH 7, being the only species in solution at the pH of 7.4 where the evaluation of the oxidant activity is performed. It is also interesting to remark, that **L2** with all propylenic

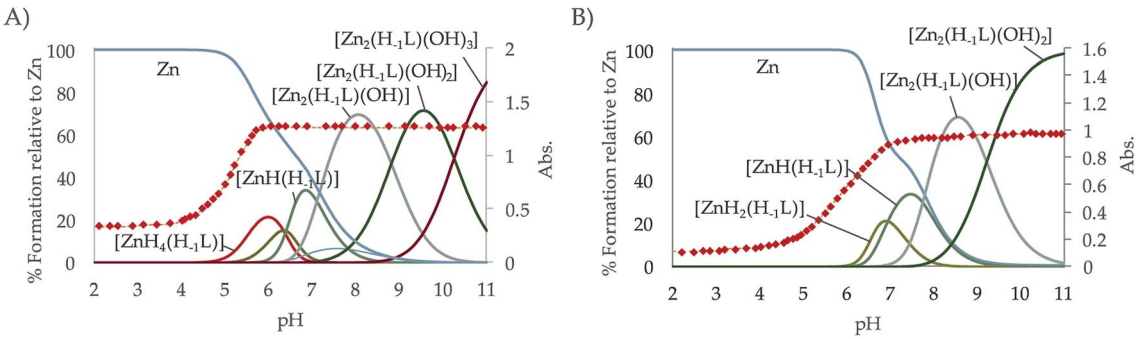

Fig. 4 Distribution diagram of the Zn^{2+} : L systems for the ligands (A) **L1** and (B) **L2** as a function of the pH in aqueous solution ($[Zn^{2+}] = 2 \times 10^{-3}$ M; $[L] = 10^{-3}$ M). The UV-Vis spectroscopic parameters of the pyridine system (red dots, $\lambda = 259$ nm for the Zn^{2+} : **L1** system and 248 nm for Zn^{2+} : **L2**) are overlaid.

chains presents more propensity to form mixed complexes than **L1**, which is likely related to the lower stability of its binary complexes.

Electrochemical studies

Cyclic voltammetry studies in solution. Since SOD activity is based on a ping-pong redox process in which the electroactive cation cycles between Cu^{2+} and Cu^{+} oxidation states, we performed cyclic voltammetric studies of our systems at pH 7.4. Fig. 6 compares the cyclic voltammetric response at glassy carbon electrode of 0.15 $NaClO_4$ aqueous solutions of the systems Cu^{2+}–**L1** and Cu^{2+}–**L2** ($[\mathbf{L}] = 10^{-3}$ M) in 1 : 1 and 2 : 1 molar ratios at pH 7.4. In the initial cathodic scan, all complexes display a similar voltammetric pattern consisting of a reduction peak at *ca.* −0.45 V *vs.* Ag/AgCl (C_1) preceded by a more or less marked shoulder around −0.30 V (C*). These peaks are followed, in the subsequent anodic scan, by an intense oxidation peak at −0.10 V (A_1) often accompanied by a shoulder near −0.25 V (A*). The oxidation signal A_1 is followed by a broad anodic wave at 0.15 V (A_{CuX}) which is coupled, in the second and successive cathodic scans, by a reduction peak at *ca.* 0.05 V (C_{CuX}).

The process A_1 has the typical characteristics of the oxidative dissolution of metals (stripping processes), whereas the signals

Table 3 Logarithms of the equilibrium constants for the interaction of Zn^{2+} with **L1**[24] and **L2** obtained by potentiometric measurements. The logarithms constants were determined in 0.15 M $NaClO_4$ at 298.1 ± 0.1 K[a]

Entry	Reaction	**L1**[24]	**L2**
1	$[CuZnH_2(H_{-1}L)]^{5+} + H^+ \rightleftarrows [CuZnH_3(H_{-1}L)]^{6+}$	—	5.58(4)
2	$[CuZnH(H_{-1}L)]^{4+} + H^+ \rightleftarrows [CuZnH_2(H_{-1}L)]^{5+}$	—	7.11(4)
3	$Cu^{2+} + Zn^{2+} + H_{-1}L^- + H^+ \rightleftarrows [CuZnH(H_{-1}L)]^{4+}$	—	33.54(5)
4	$Cu^{2+} + Zn^{2+} + H_{-1}L^- + H_2O \rightleftarrows [CuZn(H_{-1}L)(OH)]^{2+} + H^+$	19.93(5)	17.42(5)
5	$Cu^{2+} + Zn^{2+} + H_{-1}L^- + 2H_2O \rightleftarrows [CuZn(H_{-1}L)(OH)_2]^{+} + 2H^+$	12.19(3)	9.10(5)
6	$Cu^{2+} + Zn^{2+} + H_{-1}L^- + 3H_2O \rightleftarrows [CuZn(H_{-1}L)(OH)_3] + 3H^+$	1.20(7)	—

[a] Values in parentheses are standard deviations in the last significant figure.

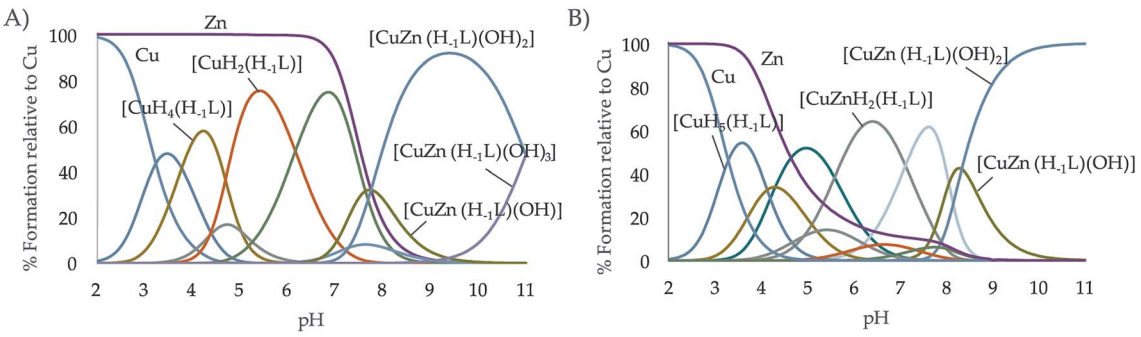

Fig. 5 Distribution diagram of the ternary systems Cu^{2+} : Zn^{2+} : L systems for the ligands (A) **L1** and (B) **L2** as a function of the pH in aqueous solution ($[Cu^{2+}] = [Zn^{2+}] = [L] = 10^{-3}$ M).

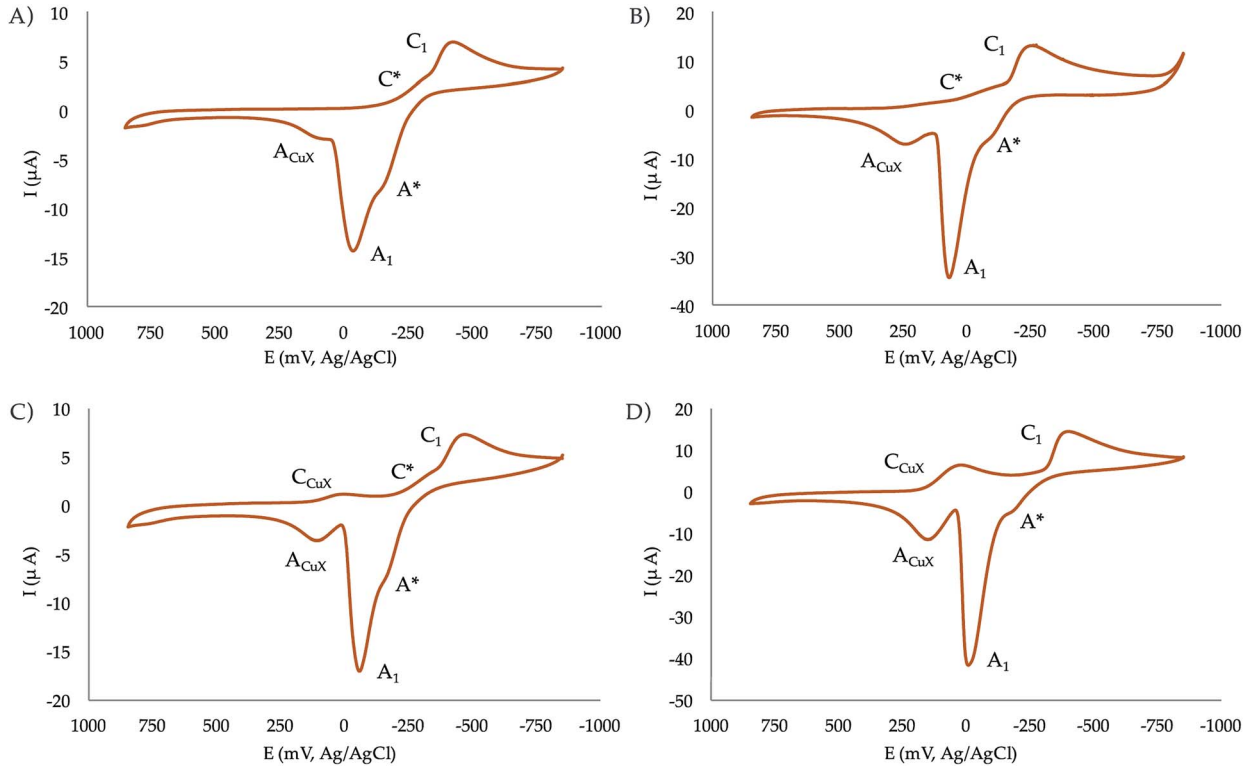

Fig. 6 Cyclic voltammograms at glassy carbon electrode of 10^{-3} M solutions of (a) Cu**L1**, (b) Cu_2**L1**, (c) Cu**L2**, (d) Cu_2**L2** in 0.15 $NaClO_4$ aqueous solutions at pH 7.4. Potential scan rate 50 mV s^{-1}.

C_{CuX}/A_{CuX} define an essentially reversible one-electron couple which can be attributed to the Cu^{2+}/Cu^{+} inter-conversion of copper–halide complexes formed as a result of the dissociation of the copper–receptor complexes during the electrochemical cycles.

When the potential range is restricted to the region between −0.10 and −0.30 V, it is possible to record a weak one-electron couple C*/A* (see Fig. S35 in the ESI†). Interestingly, the peak currents for C_1 of the mononuclear complexes is just one half that of the binuclear ones. Although the mechanism of Cu^{2+} reduction in aqueous solution can be complicated,[36–38] all these features can be interpreted in terms of the following scheme consistent with previous studies on Cu^{2+}-macrocylic[39] systems and the well-known electrochemistry of Cu^{2+}–halide complexes:[40,41]

(a) Both the mononuclear and dinuclear Cu^{2+} complexes are reduced in a two-electron process to Cu^0 *via* the process C_1.

(b) In the case of dinuclear complexes, both metal centres are reduced simultaneously and independently; *i.e.*, without electronic communication between them.

(c) The A_{CuX}/C_{CuX} couple corresponds to the one-electron reduction/oxidation of copper–halide complexes formed during electrochemical runs.

(d) The above 'principal' pathway is accompanied by a competing one involving the one-electron reduction of the parent Cu^{2+} complexes to Cu^{+}. This pathway is defined by the C*/A* couple.

This scheme means that under electrochemical conditions the predominating route is the reduction of the Cu^{2+} complexes to Cu^0. Under chemical and biochemical conditions, where different electronic and structural constraints can operate, there is possibility of the occurrence of the Cu^{2+}/Cu^{+} couple as demanded by the ROS activity of the complexes (*vide infra*). This is supported by the values of the formal redox potentials of that couple (−270 mV for Cu**L2**, −230 mV for Cu_2**L2**, −265 mV for Cu**L1**, and −140 mV for Cu_2**L1**) determined as the half-sum of the peak potentials for the C*/A* peaks.

Electrochemistry in NP-associated systems. Fig. 7 summarizes the voltammetry data recorded in Cu^{2+} solutions in the presence of suspensions of receptor-associated boehmite and silica NPs with different nominal Cu^{2+}–receptor stoichiometric ratios. The most relevant feature is the appearance of an additional cathodic signal at *ca.* −0.35 V (C_{CuL}) which can be attributed to the reduction of the NP-associated Cu^{2+}–receptor complex in the Cu^{2+} plus **BNP-L2** system and exhibits a reversible one-electron behaviour when the potential range is scanned between −0.10 to −0.40 V (see Fig. S36 in ESI†). Noticeably, the formal electrode potential of the C_{CuL}/A_{CuL} couple (−310 mV for Cu**BNP-L2** and −275 mV for Cu_2**BNP-L2**) is slightly but consistently more negative than the formal electrode potential of the equivalent process in solution phase, corresponding to the C*/A* couple in Fig. 6 and S35,† thus denoting a small relative destabilization of the copper(I) complexes upon attachment to boehmite.

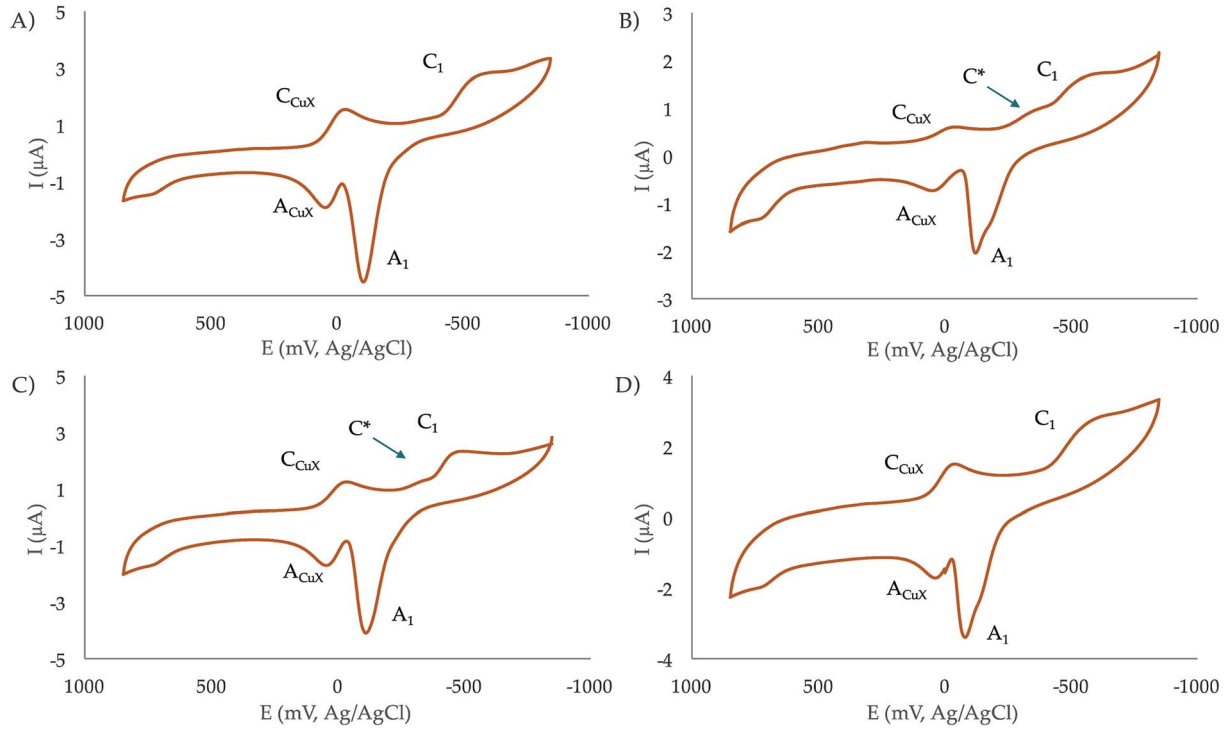

Fig. 7 Cyclic voltammograms at glassy carbon electrode of 10^{-3} M solutions of (A) Cu^{2+} (aq), (B) Cu^{2+} plus **BNP-L2** (1 : 1 molar ratio), (C) Cu^{2+} plus **BNP-L2** (2 : 1 molar ratio), (D) Cu^{2+} plus **BNP-L1** (1 : 1 molar ratio), in 0.15 $NaClO_4$ aqueous solutions at pH 7.4. Potential scan rate 50 mV s^{-1}.

Antioxidant activity

Once known the main features of the Cu^{2+} and Zn^{2+} speciation in aqueous solutions, we proceeded to evaluate the antioxidant activity of our systems. We employed an indirect method based on the side production of superoxide anions by the enzyme xanthine oxidase and their capture by the dye nitroblue tetrazolium (NBT) to give formazan. A compound displaying SOD activity will decrease the flow of superoxide radical anions and thereby, the production of formazan (see Experimental section and the representation of the fitting of the data located in ESI, Fig. S38–S41†). Blank experiments were recorded with the ligands alone without observing any effect.

The IC_{50} and k_{cat} values shown in Table 4 allow deriving several conclusions. First, the SOD activity of the copper complexes of **L1** and **L2** is remarkable (see for example the comparative of k_{cat} shown in Fig. S42†), showing the binuclear complexes much higher activity than the mononuclear ones. This can be attributed to the fact that, as above commented, the metal ion in the mononuclear complexes presents a rather saturated coordination sphere, which stabilises Cu^{2+} hampering the cycling between Cu^{2+} and Cu^{+} required for promoting the dismutation of the superoxide anions. However, since there are only seven nitrogen donors in the macrocycles, the second metal ion should be either bound to a lower number of nitrogen donors or its coordination should produce a rearrangement of the coordination spheres of both metal ions, which will be, in any case, non-saturated or completed by ancillary labile ligands, as water molecules; the first metal ion might be coordinated by the pyridine nitrogen and three neighbouring polyamine nitrogen atoms, whereas the second Cu^{2+} would be bound to the remaining three amine groups. DFT calculations for the system Cu_2–**L1** suggest the latter possibility as the most likely one (see Fig. S28†). The mixed Cu^{2+}–Zn^{2+} complexes do not show significant differences in activity with respect to the mononuclear Cu^{2+} complexes.

On the other hand, it has to be noted that none of these complexes seems to exhibit any catalase activity. The amount of H_2O_2 in solution was monitored following the evolution with time of its UV band at 229 nm (see Fig. 8 and S43†).

Table 4 Evaluation of the SOD activity of the Cu^{2+} and Cu^{2+}–Zn^{2+} systems with **L1** and **L2** at pH = 7.4, the values for the analogous complexes of pyridine are also included

System	IC_{50} (μM)	k_{cat} (10^6 M^{-1} s^{-1})
Cu–**L1**	1.4(5)[a]	2.5
CuZn–**L1**	1.6(2)	2.1
Cu_2–**L1**	0.8(1)	4.1
Cu_2–**L2**	0.37(4)	9.3
Cu_2–**BNP-L1**	0.10(3)	33.7
Cu_2–**BNP-L2**	0.12(1)	28.7
Cu_2–**SNP-L1**	3.5(3)	1.0
Cu_2–**SNP-L2**	0.45(3)	8.2
Cu_2–**L3**[b]	3.5(2)	2.4
Cu_2–**L4**[b]	0.11(2)	27.0
$Cu(ClO_4)_2$[c]	1.1(1)	2.7
CuZn–SOD[c]	0.010(2)	430

[a] Values in parenthesis are standard deviations in the last significant figure. [b] Taken from ref. 29. [c] Taken from ref. 42.

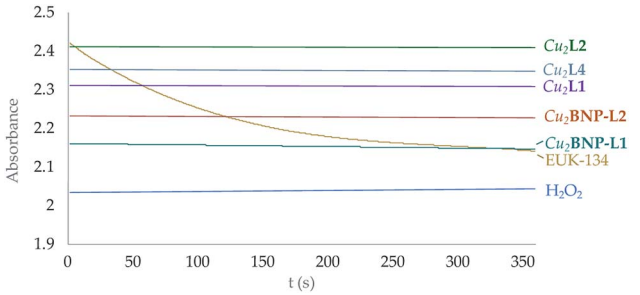

Fig. 8 Representation of the variation of the absorbance intensity with time at 219 nm of H_2O_2 solutions with the presence of both the functionalised and free Cu^{2+} complexes in solution. Yellow line corresponds to the EUK-134 reference.[12]

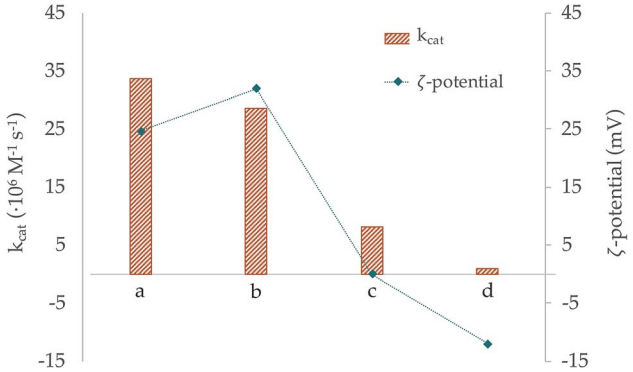

Fig. 9 Representation of the catalytic constant (orange bars) and ζ-potential (blue dots) values of the systems (a) Cu_2–**BNP-L1**, (b) Cu_2–**BNP-L2**, (c) Cu_2–**SNP-L2** and (d) Cu_2–**SNP-L1**.

However, the point of introducing a hydroxo group rightly disposed in the ligands was to permit their covalent anchorage to boehmite (γ-AlO(OH)) nanoparticles (BNPs) without loss of SOD activity. BNPs were chosen as support because we and others[43] have shown its innocuous character that has permitted its use even as co-adjuvants in vaccines.[44]

Table 4 shows that the anchoring of the binuclear complexes of the macrocycles to the BNPs leads to very significant effects with an 8-fold increase in SOD activity in the case of Cu_2–**L1**. Assays either performed with the non-grafted free NPs or with the NPs functionalised with the ligands but without the Cu^{2+} ions did not produce any activity.

This amplification of activity may be related, as previously described for other systems,[25] to the pre-concentration of Cu^{2+} complexes on the surface of the BNPs that would favour their interaction with the substrate. However, as superoxide radicals are negatively charged the charge of the surface of the NPs may also have an important contribution to the observed enhancement. Therefore, we measured the ζ-potential of the BNPs either free or functionalised with only the macrocycles or with macrocycles plus Cu^{2+} ions (Table 5, Fig. S9 and S10†). First, it has to be remarked that our 58 nm sized BNPs have a positive ζ-potential of 32.1(8) mV and that the anchorage of the macrocycles produces a slight decrease for **L1** while for the more basic and, thereby, more charged **L2**, the ζ-potential remains practically the same. Therefore, it seems that the positive charge of the NPs surface helps attracting the superoxide anions to the Cu^{2+} active centres favouring the catalytic process to occur. As noted in the introduction, this fact resembles somehow the attraction of superoxide anions exerted by the positively charged funnel of the CuZn–SOD family of enzymes.[26]

In order to double check the effect of the surface charge of the NPs we grafted our macrocycles to silica nanoparticles (SNPs) which are known to have a negatively charged surface. In our case, the ζ-potential of the free SNPs was −18.1(9) mV. This ζ-potential became less negative when the macrocycles, particularly **L2**, were anchored. Moreover, in the case of **L2** addition of two moles of Cu^{2+} per mol of ligand led to modified SNPs with a ζ-potential close to zero. The results in Tables 4, 5 and Fig. 9 show that while metal complex grafted SNPs with negative potential decrease the efficiency of superoxide dismutation, when they have potential close to zero there are not significant changes in activity with respect to the one displayed by the free metal complexes. Therefore, the results support that the electrostatic interaction between the surface of the NPs and the superoxide anionic substrates has a key role in the SOD activity increases or decreases exerted by the nanosystems.

Table 5 ζ-Potential values determined for the different nanoparticle systems. All measurements were carried out in 10^{-4} M $NaClO_4$ at pH 7.4[a]

System	ζ-Potential (mV)
BNP	32.1(8)
BNP-L1	23.9(2)
BNP-L2	35(2)
Cu_2–**BNP-L1**	24.7(1)
Cu_2–**BNP-L2**	32.0(7)
SNP	−18.1(9)
SNP-L1	−14.9(2)
SNP-L2	−5.6(2)
Cu_2–**SNP-L1**	−12(2)
Cu_2–**SNP-L2**	0(2)

[a] Values in parenthesis are standard deviations in the last significant figure.

Conclusions

The binuclear Cu^{2+} complexes of two pyridinol hexaaza-macrocycles have shown to be extremely efficient in enhancing the dismutation rate of superoxide anions into hydrogen peroxide and dioxygen (SOD activity) while they do not show any catalase activity. The high SOD activity achieved is related to the unsaturated coordination sphere that the metal centres adopt with the entry of the second metal ion. Covalent grafting of the complexes to the surface of boehmite nanoparticles show a drastic enhancement in activity that can be mainly attributed to the positive charge of the nanoparticle that would help driving the anionic substrates to the active centre reminding the role played by the positively charged funnel of

the CuZn–SOD family of enzymes. Studies performed with silica nanoparticles, which depending on the grafted molecules, show negative or close to zero ζ-potentials exhibit either decrease or similar activities to the free binuclear complexes. The studies here presented may represent an interesting to the develop nanozyme type materials with antioxidant properties.

Experimental

Synthesis and characterisation

Synthesis of the ligands. The synthesis of the compounds 4-(benzyloxy)-2,6-bis(chloromethyl)pyridine, 1,5,9,12,16,20-hexakis(ρ-tolylsulfonyl)-1,5,9,12,16,20-hexaazaicosane and 1,5,9,13,17,21-hexakis(ρ-tolylsulfonyl)-1,5,9,13,17,21-hexaazaheneicosane, precursors all of them of the macrocyclic ligands synthesised in this work, was carried out following procedures described previously in the literature.[24,28–31] **L1** was synthesised as previously described in bibliography.[24] Synthesis of **L2** was based on the same synthetic procedure used for the synthesis of **L1**, differing on the starting polyaminic chain: 1,5,9,13,17,21-hexakis(ρ-tolylsulfonyl)-1,5,9,13,17,21-hexaazaheneicosane instead of 1,5,9,12,16,20-hexakis(ρ-tolylsulfonyl)-1,5,9,12,16,20-hexaazaicosane. All reagents were obtained from commercial sources and used as received. Solvents used for the chemical synthesis were of analytical grade and used without further purification. Characterisation data of the compounds are included in the ESI (Fig. S1–S6†).

Synthesis of 1^4-benciloxy-3,7,11,15,19,23-hexakis(ρ-tolylsulfonyl)-3,7,11,15,19,23-hexaaza-1(2,6)-pyridinacyclotetracosane (1). 1,5,9,13,17,21-Hexakis(ρ-tolylsulfonyl)-1,5,9,13,17,21-hexaazaheneicosane[28,29] (2.90 g, 2.36 mmol) and K_2CO_3 (3.26 g, 23.62 mmol) were suspended in dried CH_3CN (150 cm^3). 4-(Benzyloxy)-2,6-bis(chloromethyl)pyridine[30,31] (0.80 g, 2.84 mmol) was solved in 50 cm^3 of dried CH_3CN and was added dropwise to the first suspension, over 3 h. The mixture was refluxed for 24 h and filtered. The solvent of the obtained solution was removed by vacuum evaporation and the resulting oil was purified by column chromatography (SiO_2, $CHCl_3$: CH_3OH, 97 : 3). The product was obtained as a pale yellow solid (2.10 g, yield: 62%). ^{1}H NMR (300 MHz, $CDCl_3$), δ (ppm): 7.65 (d, J = 8.1 Hz, 4H), 7.62 (d, J = 8.1 Hz, 4H), 7.56 (d, J = 8.3 Hz, 4H), 7.43–7.23 (m, 17H), 6.92 (s, 2H), 5.01 (s, 2H), 4.27 (s, 4H), 3.22 (t, J = 7.0 Hz, 4H), 3.13–2.91 (m, 16H), 2.41 (s, 6H), 2.39 (s, 6H), 2.37 (s, 6H), 2.00–1.86 (m, 2H), 1.81–1.66 (m, 8H). ^{13}C NMR (75.4 MHz, $CDCl_3$) δ (ppm): 172.18, 158.64, 143.75, 137.46, 136.73, 136.07, 135.92, 130.21, 130.14, 129.09, 128.27, 127.63, 127.57, 127.55, 70.16, 54.25, 47.83, 31.03, 30.79, 29.92, 29.52, 28.93, 21.87. MS m/z (ESI) 1458.1 ([M + Na]$^+$).

Synthesis of 3,7,11,15,19,23-hexaaza-1(2,6)-pyridinacyclotetracosan-14-ol (L2)·3HBr. 1 (2.08 g, 10.13 mmol) and phenol (12.11 g, 128.69 mmol) were solved in HBr-AcOH 33% (129 cm^3). The solution was stirred at 90 °C for further 48 h and cooled. The resulting suspension was filtered and washed several times with EtOH anhydrous to give the product **L2** in a salt form (1.15 g, yield: 88%). Characterisation data of the compound are included in the ESI (Fig. S4–S6).† ^{1}H NMR (300 MHz, D_2O), δ (ppm): 6.93 (s, 2H), 4.41 (s, 4H), 3.43–3.26 (m, 20H), 2.44–2.16 (m, 10H). ^{13}C NMR (75.4 MHz, D_2O) δ (ppm): 152.37, 110.80, 51.08, 44.95, 44.65, 44.19, 23.09, 22.67, 21.85. MS m/z (ESI) 422.2 ([M + H]$^+$). Anal. calc. for $C_{22}H_{43}ON_7 \cdot 6HBr \cdot 5.5H_2O$: C, 26.3; H, 6.0; N, 9.7: found: C, 26.4; H, 5.2; N, 9.4.

Synthesis of the nanoparticles. Boehmite nanoparticles (BNPs) were prepared by a two-step procedure already described.[32] In order to synthesise the BNPs, 146 mL of Milli-Q water were heated to 80 °C for an hour and then the aluminium *tert* butoxide (20.00 g, 81.2 mmol) was added, increasing the suspension temperature to 85 °C. One hour after, the reaction mixture was completed with the addition of 1.12 cm^3 of HNO_3. The resulting mixture was stirred for 5 days at 95 °C and then the solvent was removed by evaporation under reduced pressure. The solid was dried at 120 °C for 24 h, powdered and washed with an EtOH : H_2O 90 : 10 vol/vol mixture.

Silica nanoparticles (SNPs) were provided by deference of Drs Juan Pastor and Rafael Abargues from INTENANOMAT of the Scientific Park of the University of Valencia.

Characterization data of both the boehmite and the silica nanoparticles are included in the ESI (Fig. S7 and S8).†

Functionalisation of the boehmite and silica nanoparticles. The experimental procedure employed for grafting the ligands on the nanoparticles surface was the same for both compounds (**L1** and **L2**). To functionalise the oxidic nanoparticles 0.15 mmol of the ligand salt were suspended with 1.35 mmol of Na_2CO_3 in 20 cm^3 of ethanol, along with ∼500 mg of the nanomaterial. The mixture was refluxed for 72 h and the resulting suspension was centrifuged and washed several times with a mixture of EtOH (15 cm^3), CH_2Cl_2 (5 cm^3) and H_2O (2.5 cm^3). Characterisation data of the functionalised nanoparticles are included in the ESI (Fig. S9–S18 and Table S1).† The amount of grafted compounds was determined using elemental microanalysis and NMR calibration with an internal standard of TSP (trimethylsilylpropanoic acid); the values were $[\mathbf{L1}] = (3.5 \pm 0.4) \times 10^{-5}$ mol $g_{BNP}{}^{-1}$ and $[\mathbf{L2}] = (2.20 \pm 0.02) \times 10^{-4}$ mol $g_{BNP}{}^{-1}$ for the functionalised boehmite nanoparticles and $[\mathbf{L1}] = (2.3 \pm 0.2) \times 10^{-5}$ mol $g_{SNP}{}^{-1}$ and $[\mathbf{L2}] = (3.3 \pm 0.3) \times 10^{-5}$ mol $g_{SNP}{}^{-1}$ for the grafted silica ones. Moreover, once the NPs were reacted with copper(II) perchlorate, ICP mass spectroscopy was employed to assess the Cu^{2+} concentration. The results showed quantitative formation of the Cu^{2+} complexes.

EMF measurements

The potentiometric titrations were carried out at 298.1 ± 0.1 K using $NaClO_4$ 0.15 M as supporting electrolyte. The experimental procedure (burette, potentiometer, cell, stirrer, microcomputer *etc.*) has been fully described elsewhere.[45] The acquisition of the electromotive force (emf) data was performed with the computer program PASAT.[46] The reference electrode was an Ag/AgCl electrode in saturated KCl solution. The glass electrode was calibrated as a hydrogen ion concentration probe by titration of previously standardised amounts of HCl with CO_2-free NaOH solutions and the equivalent point determined by the Gran's method,[47,48] which gives the standard potential, E°, and the ionic product of water (pK_w = 13.73(1)). The computer program HYPERQUAD was used to calculate the

protonation and stability constants.[49] The HYSS[50] program was used to obtain the distribution diagrams. The pH range investigated was 2.5–11.0. In the binary M^{2+}/L systems the concentrations of Cu^{2+} or Zn^{2+} and the ligands ranged from 0.5 to 5 mM with M^{2+} : L molar ratios 1 : 1 and 2 : 1. In the ternary systems the Cu^{2+} : Zn^{2+} : L molar ratio was 1 : 1 : 1 with concentration of the reactants *ca.* 10^{-3} M. The titration curves for each system (at least two titrations, over 200 experimental points) were treated either as a single set or as separated curves without significant variations in the values of the stability constants. To check the consistency of the system, a final fitting of all the metal complex constants was carried out putting together all the titrations of the binary and ternary systems of a given ligand (1038 experimental points for **L1**, 778 experimental points for **L2**). The values of the constants obtained in this way agreed within the standard deviations with those retrieved from the treatment of the sets of binary and ternary systems alone.

NMR measurements

The ^{1}H and ^{13}C NMR spectra were recorded on a Bruker Advance DRX 500 spectrometer operating at 500 MHz for ^{1}H and at 100.6 MHz for ^{13}C. For the ^{13}C NMR spectra, dioxane was used as a reference standard (δ 67.4 ppm), and for the ^{1}H spectra, the solvent signal was used. Adjustments to the desired pH were made using drops of DCl or NaOD solutions. The pD was calculated from the measured pH values using the correlation, pH = pD − 0.4.[51]

UV-Vis measurements

The solvents used were of spectroscopic or equivalent grade. Water was twice distilled and passed through a Millipore apparatus. The pH values were measured with a Metrohm 713 pH meter and adjustments of the hydrogen ion concentration of the solutions were made with diluted HCl and NaOH solutions. UV-Vis absorption spectra were recorded with an Agilent 8453 spectrometer.

Electrochemical measurements

Cyclic voltammetric experiments in 10^{-3} M aqueous solutions of the receptors in the presence of different stoichiometric concentrations of Cu^{2+} were studied using 0.15 M $NaClO_4$ as a supporting electrolyte. The pH was adjusted to 7.4 adding appropriate amounts of $HClO_4$ and NaOH solutions. Electrochemical experiments were performed with a CHI 440 potentiostatic device using a conventional three-compartment cell with a Ag/AgCl (3 M NaCl) reference electrode, a platinum wire auxiliary electrode and a glassy-carbon working electrode (geometrical area 0.071 cm^2). Prior to each voltammetric run, the electrode was polished with an aqueous suspension of alumina on a soft surface, rinsed with water and dried.

ζ-Potential determination

The electric potential of the interfacial surface between the nanoparticles and the dispersion medium, also known as ζ-potential, was measured using a Malvern Mastersizer 2000 instrument. Solutions containing 1 mg of the NPs in 10 cm^3 of a 10^{-4} M $NaClO_4$ aqueous solution at pH 7.4 were employed in the measurements.

Density functional theory (DFT) calculations

DFT calculations of the Cu^{2+} complexes were performed with DFT as a computational method using UB3LYP/6-311+G* and UB3LYP/LANDL2DZ combinations. Specifically, the 6-311+G* basis set was used for the nonmetallic atoms, while the LANDL2DZ was used for the transition metals, in which it has been generated *ab initio* effective core potentials to replace the Coulomb, core orthogonality, and exchange effects of the chemically inert core electrons in Cu^{2+}. The Gaussian 09 (ref. 52) package was used for these DFT calculations and the Molden[53] and Pymol[54] package for the modelling analysis. The aqueous environment was implicitly considered by using the Self-Consistent Reaction Field (SCRF) method with a model of continuous polarization model with water as a solvent (Polarizable Continuum Model – PCM).[55–57]

In vitro McCord–Fridovich SOD activity assays

SOD-like activity was determined by using the nitro blue tetrazolium (NBT) method.[58–61] The assays were carried out in a pH = 7.4 50 mM HEPES buffer at 298 K. The xanthine (2.2×10^{-4} M) and xanthine oxidase system was used to generate a reproducible and constant flux of superoxide anions. The rate of reduction of NBT (7.3×10^{-5} M) to blue formazane was followed spectrophotometrically at 560 nm. Data in the absence of the complex were used as a reference. The rate of NBT reduction was progressively inhibited after the addition of the complex solutions at increasing concentrations prepared in 50 mM Tris–HCl buffer. The percentage of inhibition of the NBT reduction was used as a measure of the SOD activity of the compounds. The concentration of complex required to yield 50% inhibition of NBT reduction (IC_{50}) was determined from a plot of percentage inhibition *versus* complex concentration. The IC_{50} data have been calculated from the mean values of (at least) three independent measurements. The catalytic constant was calculated from the IC_{50} using the equation $k_{cat} = k_{NBT}[NBT]/IC_{50}$ where $k_{NBT} = (5.9 + 0.5) \times 10^5$ M^{-1} s^{-1}.[62–64]

Conflicts of interest

There are no conflicts to declare.

Acknowledgements

We acknowledge the financial support by the Spanish MINECO and FEDER funds from the European Union (Project CTQ2016-78499-C6-1-R, CTQ2017-90852-REDC and Unidad de Excelencia María de Maeztu MDM-15-0538) and Generalitat Valenciana (PROMETEO II 2015-002). A. M.-C. wants to thank Spanish Ministry of Science, Research and Universities for the PhD grant FPU14/05098. We also acknowledge Mass Spectrometry, and

NMR service from the Central Services for Experimental Research (SCSIE) of University of Valencia.

References

1 V. Dias, E. Junn and M. M. Mouradian, *J. Parkinson's Dis.*, 2013, **3**, 461.
2 V. Chauhan and A. Chauhan, *Pathophysiology*, 2006, **13**, 195.
3 A. Kumar and R. R. Ratan, *J. Huntington's Dis.*, 2016, **5**, 217.
4 Z. Liu, T. Zhou, A. C. Ziegler, P. Dimitrion and L. Zuo, *Oxid. Med. Cell. Longevity*, 2017, **2017**, 1.
5 I. A. Abreu and D. E. Cabelli, *Biochim. Biophys. Acta*, 2010, **1804**, 263.
6 V. B. Djordjević, *Int. Rev. Cytol.*, 2004, **237**, 57.
7 C. D. Putnam, A. S. Arvai, Y. Bourne and J. A. Tainer, *J. Mol. Biol.*, 2000, **296**, 295.
8 S. Gandhi and A. Y. Abramov, *Oxid. Med. Cell. Longevity*, 2012, **2012**, 1.
9 L. E. Scott and C. Orvig, *Chem. Rev.*, 2009, **109**, 4885.
10 M. T. Fodero-Tavoletti, V. L. Villemagne, C. C. Rowe, C. L. Masters, K. J. Barnham and R. Cappai, *Int. J. Biochem. Cell Biol.*, 2011, **43**, 1247.
11 J. M. McCord and M. A. Edeas, *Biomed. Pharmacother.*, 2005, **59**, 139.
12 I. Ivanović-Burmazović and M. R. Filipović, *Adv. Inorg. Chem.*, 2012, **64**, 53.
13 P. A. Adlard, R. A. Cherny, D. I. Finkelstein, E. Gautier, E. Robb, M. Cortes, I. Volitakis, X. Liu, J. P. Smith, K. Perez, K. Laughton, Q.-X. Li, S. A. Charman, J. A. Nicolazzo, S. Wilkins, K. Deleva, T. Lynch, G. Kok, C. W. Ritchie, R. E. Tanzi, R. Cappai, C. L. Masters, K. J. Barnham and A. I. Bush, *Neuron*, 2008, **59**, 43.
14 E. Crabb and E. A. Moore, *Metals and Life*, Royal Society of Chemistry, 2010.
15 K. Aston, N. Rath, A. Naik, U. Slomczynska, O. F. Schall and D. P. Riley, *Inorg. Chem.*, 2001, **40**, 1779.
16 G.-F. Liu, M. Filipović, F. W. Heinemann and I. Ivanović-Burmazović, *Inorg. Chem.*, 2007, **46**, 8825.
17 M. Tamura, Y. Urano, K. Kikuchi, T. Higuchi, M. Hirobe and T. Nagano, *J. Organomet. Chem.*, 2000, **611**, 586.
18 I. Szilágyi, I. Labádi, K. Hernadi, I. Pálinkó, N. V. Nagy, L. Korecz, A. Rockenbauer, Z. Kele and T. Kiss, *J. Inorg. Biochem.*, 2005, **99**, 1619.
19 P. Failli, D. Bani, A. Bencini, M. Cantore, L. Di Cesare Mannelli, C. Ghelardini, C. Giorgi, M. Innocenti, F. Rugi, A. Spepi, R. Udisti and B. Valtancoli, *J. Med. Chem.*, 2009, **52**, 7273.
20 O. Singh, N. Tyagi, M. M. Olmstead and K. Ghosh, *Dalton Trans.*, 2017, **46**, 14186.
21 M. P. Clares, S. Blasco, M. Inclán, L. del Castillo Agudo, B. Verdejo, C. Soriano, A. Doménech, J. Latorre and E. García-España, *Chem. Commun.*, 2011, **47**, 5988.
22 J. González-García, Á. Martínez-Camarena, B. Verdejo, M. P. Clares, C. Soriano, E. García-España, H. R. Jiménez, A. Doménech-Carbó, R. Tejero, E. Calvo, L. Briansó-Llort, C. Serena, S. Trefler and A. García-España, *J. Inorg. Biochem.*, 2016, **163**, 230.
23 L. Guijarro, M. Inclán, J. Pitarch-Jarque, A. Doménech-Carbó, J. U. Chicote, S. Trefler, E. García-España, A. García-España and B. Verdejo, *Inorg. Chem.*, 2017, **56**, 13748.
24 Á. Martínez-Camarena, E. Delgado-Pinar, C. Soriano, J. Alarcón, J. M. Llinares, R. Tejero and E. García-España, *Chem. Commun.*, 2018, **54**, 3871.
25 C. Fasting, C. A. Schalley, M. Weber, O. Seitz, S. Hecht, B. Koksch, J. Dernedde, C. Graf, E. W. Knapp and R. Haag, *Angew. Chem., Int. Ed.*, 2012, **51**, 10472.
26 I. Bertini, S. Manganl and M. S. Viezzoli, *Adv. Inorg. Chem.*, 1998, **45**, 127.
27 J. E. Richman and T. J. Atkins, *J. Am. Chem. Soc.*, 1974, **96**, 2268.
28 B. Dietrich, M. W. Hosseini, J.-M. Lehn and R. B. Sessions, *Helv. Chim. Acta*, 1983, **66**, 1262.
29 R. Belda, S. Blasco, B. Verdejo, H. R. Jiménez, A. Doménech-Carbó, C. Soriano, J. Latorre, C. Terencio and E. García-España, *Dalton Trans.*, 2013, **42**, 11194.
30 E. Busto, A. González-Álvarez, V. Gotor-Fernández, I. Alfonso and V. Gotor, *Tetrahedron*, 2010, **66**, 6070.
31 P. Froidevaux, J. M. Harrowfield and A. N. Sobolev, *Inorg. Chem.*, 2000, **39**, 4678.
32 R. Aucejo, P. Díaz, E. García-España, J. Alarcón, E. Delgado-Pinar, F. Torres, C. Soriano and M. C. Guillem, *New J. Chem.*, 2007, **31**, 44.
33 J. Aguilar, M. G. Basallote, L. Gil, J. C. Hernández, M. A. Máñez, E. García-España and B. Verdejo, *Dalton Trans.*, 2004, 94.
34 A. Bencini, A. Bianchi, E. García-España, M. Micheloni and J. A. Ramirez, *Coord. Chem. Rev.*, 1999, **188**, 97.
35 W. R. Harris, K. N. Raymond and F. L. Weitl, *J. Am. Chem. Soc.*, 1981, **103**, 2667.
36 F. M. Hawkridge and H. H. Bauer, *Anal. Chem.*, 1972, **44**, 364.
37 J. L. Anderson and I. Shain, *Anal. Chem.*, 1976, **48**, 1274.
38 J. L. Anderson and I. Shain, *Anal. Chem.*, 1978, **50**, 163.
39 A. Doménech, E. García-España, S. V. Luis, V. Marcelino and J. F. Miravet, *Inorg. Chim. Acta*, 2000, **299**, 238.
40 G. Gunawardena, G. Hills and I. Montenegro, *J. Electroanal. Chem.*, 1985, **184**, 357.
41 J. Crousier and I. Bimaghra, *Electrochim. Acta*, 1989, **34**, 1205.
42 H. Ohtsu, Y. Shimazaki, A. Odani, O. Yamauchi, W. Mori, S. Itoh and S. Fukuzumi, *J. Am. Chem. Soc.*, 2000, **122**, 5733.
43 A. Rutenberg, V. V. Vinogradov and D. Avnir, *Chem. Commun.*, 2013, **49**, 5636.
44 B. Sun and T. Xia, *J. Mater. Chem. B*, 2016, **4**, 5496.
45 E. Garcia-Espana, M. J. Ballester, F. Lloret, J. M. Moratal, J. Faus and A. Bianchi, *J. Chem. Soc., Dalton Trans.*, 1988, **2**, 101.
46 M. Fontanelli and M. Micheloni, *Proceedings of the I Spanish-Italian Congress on Thermodynamics of Metal Complexes*, Peñíscola, España, 1990.
47 G. Gran, *Analyst*, 1952, **77**, 661.
48 F. J. C. Rossotti and H. Rossotti, *J. Chem. Educ.*, 1965, **42**, 375.
49 P. Gans, A. Sabatini and A. Vacca, *Talanta*, 1996, **43**, 1739.
50 L. Alderighi, P. Gans, A. Ienco, D. Peters, A. Sabatini and A. Vacca, *Coord. Chem. Rev.*, 1999, **184**, 311.

51 A. K. Covington, M. Paabo, R. A. Robinson and R. G. Bates, *Anal. Chem.*, 1968, **40**, 700.

52 M. J. Frisch, G. W. Trucks, H. B. Schlegel, G. E. Scuseria, M. A. Robb, J. R. Cheeseman, G. Scalmani, V. Barone, B. Mennucci, G. A. Petersson, H. Nakatsuji, M. Caricato, X. Li, H. P. Hratchian, A. F. Izmaylov, J. Bloino, G. Zheng, J. L. Sonnenberg, M. Hada, M. Ehara, K. Toyota, R. Fukuda, J. Hasegawa, M. Ishida, T. Nakajima, Y. Honda, O. Kitao, H. Nakai, T. Vreven, J. A. Montgomery Jr, J. E. Peralta, F. Ogliaro, M. Bearpark, J. J. Heyd, E. Brothers, K. N. Kudin, V. N. Staroverov, T. Keith, R. Kobayashi, J. Normand, K. Raghavachari, A. Rendell, J. C. Burant, S. S. Iyengar, J. Tomasi, M. Cossi, N. Rega, J. M. Millam, M. Klene, J. E. Knox, J. B. Cross, V. Bakken, C. Adamo, J. Jaramillo, R. Gomperts, R. E. Stratmann, O. Yazyev, A. J. Austin, R. Cammi, C. Pomelli, J. W. Ochterski, R. L. Martin, K. Morokuma, V. G. Zakrzewski, G. A. Voth, P. Salvador, J. J. Dannenberg, S. Dapprich, A. D. Daniels, O. Farkas, J. B. Foresman, J. V. Ortiz, J. Cioslowski and D. J. Fox, *Gaussian 09, Version C.01*, 2009.

53 G. Schaftenaar and J. H. Noordik, *J. Comput.-Aided Mol. Des.*, 2000, **14**, 123.

54 Schrödinger-LLC, *The PyMOL Molecular Graphics System Version 1.8*.

55 S. Miertuš, E. Scrocco and J. Tomasi, *Chem. Phys.*, 1981, **55**, 117.

56 J. L. Pascual-ahuir, E. Silla and I. Tuñon, *J. Comput. Chem.*, 1994, **15**, 1127.

57 M. Cossi, G. Scalmani, N. Rega and V. Barone, *J. Chem. Phys.*, 2002, **117**, 43.

58 L. W. Oberley and D. R. Spitz, *Oxygen Radicals in Biological Systems*, Elsevier, 1984.

59 L. W. Oberley and D. R. Spitz, *Handbook of methods of oxygen radicals research*, CRC Press, Boca Raton, USA, 1986.

60 C. Beauchamp and I. Fridovich, *Anal. Biochem.*, 1971, **44**, 276.

61 J. Y. Zhou and P. Prognon, *J. Pharm. Biomed. Anal.*, 2006, **40**, 1143.

62 B. H. J. Bielski and H. W. Richter, *J. Am. Chem. Soc.*, 1977, **99**, 3019.

63 R. F. Pasternack and B. Halliwell, *J. Am. Chem. Soc.*, 1979, **101**, 1026.

64 S. Durot, C. Policar, F. Cisnetti, F. Lambert, J.-P. Renault, G. Pelosi, G. Blain, H. Korri-Youssoufi and J.-P. Mahy, *Eur. J. Inorg. Chem.*, 2005, 3513.

